Quantifying Indonesia's nitrous oxides (NO_x) emissions hotspots using satellite observations

Version 1.0

August 2026

Prepared by:
Rosa Gierens, Data Lead

Contributors: Hubert Thieriot, Danny Hartono

Disclaimer

Satellite measurements to strengthen environmental governance

Indonesia's environmental governance is hampered by a lack of data transparency, particularly regarding industrial emissions. Despite mandatory Continuous Emissions Monitoring Systems (CEMS) and Environmental Impact Assessments (EIAs), the government has largely withheld crucial emissions data. Satellite-based earth observation offers objective, non-intrusive, and consistent environmental data with broad spatial and temporal coverage. Satellite-based methods for detecting and estimating emissions of gaseous air pollutants are well established and provide an independent data source that can complement and verify official records.

To support transparent and open emission monitoring, CREA has generated a dataset that maps out major NO_X emission point sources and their emissions in Indonesia. Satellites provide NO_2 measurements at a spatial resolution of 3.5-5.5 km with an uncertainty of 25-60% (Lange et al., 2023, 2024). While a ~5 km resolution is insufficient to pinpoint individual trucks or smokestacks, it is possible to identify large power plants, polluted cities, and heavily trafficked ship routes. By combining satellite observations with other atmospheric data (most importantly, wind) and applying modelling tools, NO_X emissions can be quantified.

Unfortunately, satellite measurements are not possible under all conditions; for example, clouds often cause gaps in the satellite data. This is in particular a problem in Indonesia, which, as is typical in the wet tropics, has high cloud cover. The relatively high uncertainty of a single observation as well as the gaps in the measurements can be mitigated by combining data from several satellite overflights. Although a single image is noisy and it might be hard to detect anything but the largest polluters, reviewing several months or years of data together leads to clear signals to exploit.

This document provides a brief introduction to the method applied, details the implementation and datasets, and evaluates the performance of the implemented approach.

Flux divergence method to detect and estimate NO_X emissions from point sources

To select an approach for estimating NO_X emissions, we sought a method that leverages the high-resolution capabilities of latest air-quality satellites while being sufficiently mature to allow implementation with minimal development overhead. Furthermore, the required data needs to be accessible and cover the geographical areas of interest. We chose to use the flux divergence method (Beirle et al., 2019), which is a physical method for determining emissions of short-lived gases from point sources. The flux divergence method is relatively lightweight to compute, and it relies on a limited number of datasets, making it suitable for CREA's needs.

Methodology

The flux divergence approach is based on the continuity equation, which states that in steady state, the net transport through an atmospheric column (i.e., the divergence of the horizontal flux) equals the balance of emissions and sinks within that column. Formally, this is written as

$$\nabla F = e - s \tag{1}$$

where ∇F is the horizontal flux divergence, e contains all emissions, and s contains the sinks within the column. Neglecting the divergence of the wind field, the horizontal flux divergence (∇F) is equal to advection (A), so that Eq. 1 becomes

$$e = A + s = \boldsymbol{u} \cdot (\nabla V) + s \tag{2}$$

where $\boldsymbol{u}$ is the horizontal wind vector, and V is the tropospheric vertical column density (TVCD) of NO_X. Sun (2022) noted that in the presence of orography, the vertical flux near the surface cannot be ignored, and derived the following equation for spatio-temporal averages:

$$e = \boldsymbol{u} \cdot (\nabla V) + X(V\boldsymbol{u}_0 \cdot (\nabla z_0)) + s \tag{3}$$

where X is a scaling height to estimate surface NO_X concentration, $\boldsymbol{u_0}$ is the near-surface wind, and z_0 is the surface elevation. Here, the second term accounts for the effects of orography, and Beirle et al. (2023) demonstrated that including this term resulted in a considerable reduction of artefacts in the vicinity of mountains. Following the notation of Beirle et al., (2023), here the first two terms in Eq. 3 are referred to as the topography-corrected advection (A^*). For a detailed discussion of the theoretical basis of the method, see Beirle et al. (2023), Koene et al. (2024), and Sun (2022).

In practice, the topography-corrected advection is calculated for each satellite swath on the native grid of the L2 satellite data (Beirle et al., 2023; de Foy & Schauer, 2022). The data is then interpolated to a regular grid and temporally averaged. Point sources are identified by searching for local maxima in the temporal mean A^* field, and the emission rates for selected sources are calculated by integrating over a 15-km radius around the source. The integration over the area is required as the varying resolution of the satellite data and the numerical methods used lead to broadening of the advection peak.

Instead of estimating a sink term for Eq. 3, Beirle et al. (2023) updated the approach to account for the NO_X sink. During sunny daytime conditions, which are required for the satellite measurements, the tropospheric NO_X sink is dominated by the chemical loss. Thus, the sink can be estimated assuming a first-order lifetime (τ). It then follows that the amount of NO_X along the plume decreases exponentially with time, while the magnitude of the NO_X sink depends on the amount of NO_X and, consequently, on the magnitude of the NO_X emission. The effect of the NO_X sink within the integrated area used for estimating the point source emission (E) can therefore be included as a multiplication factor to the integrated advection:

$$E = exp\left(\frac{t_r}{\tau}\right) \cdot \int_{o} A^* \; dA \qquad (4)$$

where t_r is the residence time within the integration area, and τ is the NO_X lifetime. The residence time is calculated simply from the integration radius and mean wind speed, and the NO_X lifetime is calculated as $\tau = 1.0089 \times \exp(0.0242 \times (|\mathrm{lat}| + 9.6024))$ (Beirle et al., 2023; Lange et al., 2022).

Scaling NO_2 to NO_X

NO_X consists of both NO and NO_2, but the satellite only measures NO_2. Following Beirle et al. (2023), the NO_2 TCVD is scaled to NO_X TCVD using a conversion factor based on photostationary steady state:

$$L = \frac{[NOx]}{[NO2]} = 1 + \frac{J}{k\,[O_3]} \quad (5)$$

where J is the photolysis frequency of NO_2, estimated as $J = 0.01667 \times \exp(-0.575/\cos(\theta))\ s^{-1}$ (Dickerson et al., 1982), and k is the reaction rate constant of NO and O_3, calculated as $k = 2.07 \times 10^{-12} \times \exp(-1400/T)\ cm^3\ molec^{-1}\ s^{-1}$ (IUPAC, 2013). Here, θ denotes the solar zenith angle, and T represents the temperature. The omission of the effects of Volatile Organic Compounds (VOCs) is considered negligible, as the NO_X concentrations at the point source locations are high.

Datasets

All datasets were obtained over the period from 1 May 2018 (the start of satellite data availability) to 31 December 2025. To derive NO_X emissions for Indonesia, data were obtained for a bounding box covering the area from 12°S, 94°E to 9°N, 143°E. For evaluating the performance of the methodology, data for the contiguous United States was also collected for an area defined from 24°N, 126°W to 50°N, 64°W.

Satellite data: TROPOMI NO_2

For the satellite data, we used the L2 NO_2 product from TROPOMI onboard the Sentinel 5P satellite (European Space Agency, 2021). During the mission, the NO_2 retrieval algorithm has received several updates. To ensure the consistency of the dataset, we used the collection 03 data, which corresponds to the RPRO data stream until 25 July 2022 and the OFFL data stream afterwards. The data is obtained from the Copernicus Data Space Ecosystem (D.Kovács et al., 2026), and is used here following the free, full, and open access granted by Copernicus (European Comission, n.d.). In addition to the NO_2 TVCD and associated data quality parameters, the dataset also contains surface elevation and surface wind speed, needed for calculating the topographic correction for advection, and the solar zenith angle, used for the NO_2:NO_X scaling (see Methodology for details).

Reanalysis data: ERA5 and CAMS

For the horizontal wind required for calculating the NO_X advection, we used data from the ERA5 reanalysis (Copernicus Climate Change Service, 2023). We downloaded the hourly wind data at model levels at a 0.25°x0.25° horizontal resolution and interpolated the wind components from the model levels to 500 m above the ground. The wind at 500 m was then linearly interpolated to the TROPOMI orbit time and L2 grid.

Atmospheric composition from the Copernicus Atmosphere Monitoring Service (CAMS) global reanalysis (Copernicus Atmosphere Monitoring Service, 2020a; Inness et al., 2019) was used to obtain surface-level ozone data needed for the NO_2:NO_X scaling. The ozone mass mixing ratio was converted to concentration using the ideal gas law for dry air, utilising the pressure and temperature available in the CAMS reanalysis dataset. We used the monthly average product (Copernicus Atmosphere Monitoring Service, 2020b), available at 3-hourly resolution and 0.75°x0.75° horizontal resolution and took the values at the lowest model level to derive the scaling factor. The ozone concentration was then linearly interpolated to TROPOMI orbit time-of-day and L2 grid.

Reference emissions data

To evaluate the performance of the satellite-based emission estimates, we used bottom-up NO_X emission data as "ground truth". We used data provided by the US Environmental Protection Agency, containing NO_X emissions for power plants, publicly available from the Clean Air Markets Program Data (United States Environmental Protection Agency (EPA), n.d.). For all units listed, we merged the units that were located in the same location and considered these as single facilities for the comparison with the satellite-based emission data.

Implementation

The implementation follows the flux divergence method as described by Beirle et al. (2023), hereafter B23, with some minor modifications. For brevity, we focus here on the updates we made, and unless otherwise mentioned, the methods follow B23.

Calculation of the advection fields

To obtain emission rate estimates in areas with low TROPOMI NO_2 data coverage, we added a noise reduction step at the beginning of the process. Reducing noise in the L2 NO_2 data allows us to lower the temporal data coverage requirement for the temporally averaged advection. Thus, we could expand the area covered by the averaged advection data. As a trade-off, the NO_2 maxima, and consequently the NO_X advection maxima, are less pronounced. For image denoising, we applied a Wiener filter to the L2 NO_2 TVCD data, using a window size of 3×3 and a noise level of 2.95×10^{-10} mol/m^2.

To ensure the quality of the data used, only TROPOMI NO_2 data is included where the QA > 0.75, and solar zenith angle < 65. Unlike Beirle et al. (2023), we don't limit the viewing zenith angle in order to increase the sparse data coverage over Indonesia. We also omit the air mass factor correction, as in our evaluation we did not find that it contributed to a notable improvement in the accuracy of the results. Otherwise, after applying the Wiener filter, the calculations follow the same steps as described by B23: scaling NO_2 to NO_X, transforming the wind vector to the TROPOMI grid, calculating the topography-corrected advection, and filtering the data based on the quality criteria and wind speed threshold.

In the next step, the data is linearly interpolated to a regular grid, and the temporal mean at each grid point is calculated. B23 applied a 10% data coverage threshold at each grid point for the calculation of the temporal mean. As a result of the noise reduction performed on the NO_2 data, we found that only seven data points are sufficient to get a reasonable mean advection value. However, with such a low number of data points, single outliers can significantly influence the mean value. To mitigate this issue, we removed outliers from the time series of each pixel using the median absolute deviation filter with a threshold value of 3.5 before calculating the temporal average advection.

Point source detection

For identifying NO_X point sources, the topography-corrected advection (*A**, in the following simply advection) was interpolated and temporally averaged on a regular latitude-longitude grid with 0.025° resolution, as in B23. Point sources were detected by iteratively searching for the maxima in the *A** field, checking the source candidate against selected criteria (detailed below), setting a mask to True for all pixels with positive advection values in a 15 km radius around the maxima (30 km in case of negative values detection), and then continuing with the next iteration. In all iterations, the advection maxima were searched from unmasked (e.g. mask == False) areas. This is a slightly different approach than what was done by B23, who, instead of keeping a separate mask, simply set the positive values in the advection data to nan in the 15 km (30 km) radius.

In the B23 approach, subsequent iterations increasingly yielded the category "gap", as more and more of the advection map is missing in each iteration. We wanted to distinguish between source candidates that are discarded because of the lack of satellite data availability, which is common in Indonesia, and source candidates that result in gaps because other sources nearby have been detected. This created situations where advection maxima were detected at edges of distributed sources which did not exhibit any local maxima. In the B23 approach, these cases would have been considered gaps. For this reason, we added an additional check for source candidates where no true local maxima is detected.

In the point source detection, the source candidates were checked for:

1. Following B23, if the source candidate is within 30 km of the edge of the domain (see domain definition above), it is discarded.
2. Data coverage: if more than 25% of the pixels within a 15 km radius from the advection maxima are missing, the candidate is discarded. Note that pixels are set to missing if less than seven data points are available for calculating the temporally averaged value for the pixel.
3. In some cases, assumptions made for the flux divergence around the transport of NOx are invalid and result in artefacts with a dipole pattern, i.e. a pair of positive and negative advection. Following B23, we look for the magnitude of the negative values in a 30 km radius around an advection maximum, and if the negative values are as large or larger in magnitude compared to the positive maxima the source candidate is discarded. In this case, the 30 km radius is also masked from further iterations.
4. To filter out narrow spikes, which are considered artefacts, the peak area fraction as described in B23 is calculated. Candidates with a peak area fraction below 0.3 are excluded.
5. To further filter out suspicious high values in the NO_X advection field, we added a criterion to check for the average NO_X TVCD within a 15 km radius. The rationale is that for a point source to be present, at least some amount of NO_X is expected to be present at the source location. Candidates with NO_X TVCD below 0.5e-6 kg/m^2 are discarded.
6. In contrast to B23, the area sources are not detected based on the peak area fraction, because it was difficult to find a suitable threshold. The addition of the low-pass filtering and possibly the omission of the AMF correction led to the point sources being less pronounced and thus harder to automatically distinguish from distributed sources. Instead, we do the following:
    a. Check that the source candidate presents a local maximum in the advection field. In practice, the maximum value in the unmasked advection within a 15 km radius from the detected source candidate is searched. If the maximum is more than 10 km away from the detected candidate location, it is considered that the source candidate does not represent a local maximum, and the candidate is discarded.

b. We compare the average advection within the 15-km integration area with the average advection in the "background area", which we defined as the annulus of 15-km and 17-km circles around the source candidate. If the ratio of the mean advection in the background area and the integration area is above 0.7, the candidate is discarded.

7. Following B23, source candidates for which the topographic wind term contributes over 50% of the emission are discarded.
8. Finally, the source needs to be large enough to be considered significant. Candidates where the final emission estimate is below the detection limit of 0.055 kg/s are labelled as "Below detection limit". This lower threshold value, corresponding to 50% of the detection limit defined by Beirle et al. (2019), is used at this stage to avoid prematurely excluding potential point sources.

In contrast to B23, the temporal persistence of the point sources was not considered in order to include sources that are present only part of the evaluation period. Also, the relative error criterion was omitted for simplicity.

The point source detection with the above-listed settings is run for the advection field averaged over the years 2018-2025, 2019-2025, 2020-2025, 2021-2025, 2022-2025, 2023-2025, and 2024-2025. For each time period, up to 1,000 iterations were performed. The iteration is stopped if no maximum above the threshold of 0.5e-10 $kg/m^2/s$ is found. Running different time periods was done to maximise the detection of point sources. The aim is to both detect sources that might be present only part of the evaluation period, as well as sources for which multiple years are needed to collect enough samples while maximising the detection of sources that have appeared during the last few years. All detections that pass all filters listed above are considered source candidates.

Next, the source candidates were filtered to only include points in Indonesia. Then the results from all of the different detection runs were combined, and all duplicate source candidates were dropped. Several candidates were almost next to each other, and all candidates closer than 10 km from each other were joined. For the joined candidates, the location was defined as the centroids of the merged geometries. This resulted in a list of potential point sources, to be verified in the next step.

Point source NO_x emission calculation

For all potential point sources, daily rasters were calculated on a local UTM grid at 1 km resolution, centred on each source. The UTM coordinates are used instead of latitude and longitude to avoid grid distortions, and upsampling is used to better preserve the observational footprint and improve visualisations.

Because the locations of potential point sources were derived on a coarser grid and also changed when joining with nearby neighbours, the locations of the point sources were first updated. The source location is defined as the grid pixel with the maximum advection value in the temporal mean within a 20 km × 20 km domain centred around the potential point source. If the distance to the maximum advection value exceeds 10 km from the source candidate location detected on the coarse grid, the point source was discarded. Furthermore, if the distance between two point sources was less than 15 km, the source with the lower maximum advection value was dropped. This process ensured that all detected point sources present true local maxima, and that the reported point source locations align with the data used for the emission calculation.

Following B23, NO_X emissions were calculated for each detected point source by a simple interpolation over a 15 km radius, and the lifetime correction was applied (see Methodology). The emission estimates were calculated for averaging periods of 1, 2, 3 and 4 years, as well as all years (2018-2025). For consistency, the same criteria used for the initial point source detection, listed above, were applied to all emission estimates, with some thresholds tightened to ensure the accuracy of the results. Emissions below 0.11 kg/s, with the topographic wind fraction over 0.4, and with the maximum negative value within a 30 km radius being over 0.5 of the maximum advection value, were set to missing values.

Point sources that have no valid emission estimates for any of the temporal averaging periods were omitted from the list of point sources. Finally, the point sources were manually checked, and 3 point sources were dropped.

In addition to NO_X emission estimates, the area in which advection exceeds 0.75*maximum value was defined for each point source, and used to match the detected point sources with infrastructure data to identify polluters.

Evaluation

Point source detection

A total of 29 NO_x point sources were identified in Indonesia. The B23 catalogue includes nine point sources in Indonesia (Figure 1). The CREA analysis detected all the same point sources as B23 except for one. This point was also identified by our point-source detection algorithm but discarded due to too-large negative advection values found within the 30-km radius. Some of the point sources detected in the CREA analysis have only appeared in recent years and did not exist during the period covered by the B23 analysis, which covered 2018-2021. Additional detections in the CREA analysis were enabled by extending it to areas with lower data coverage.

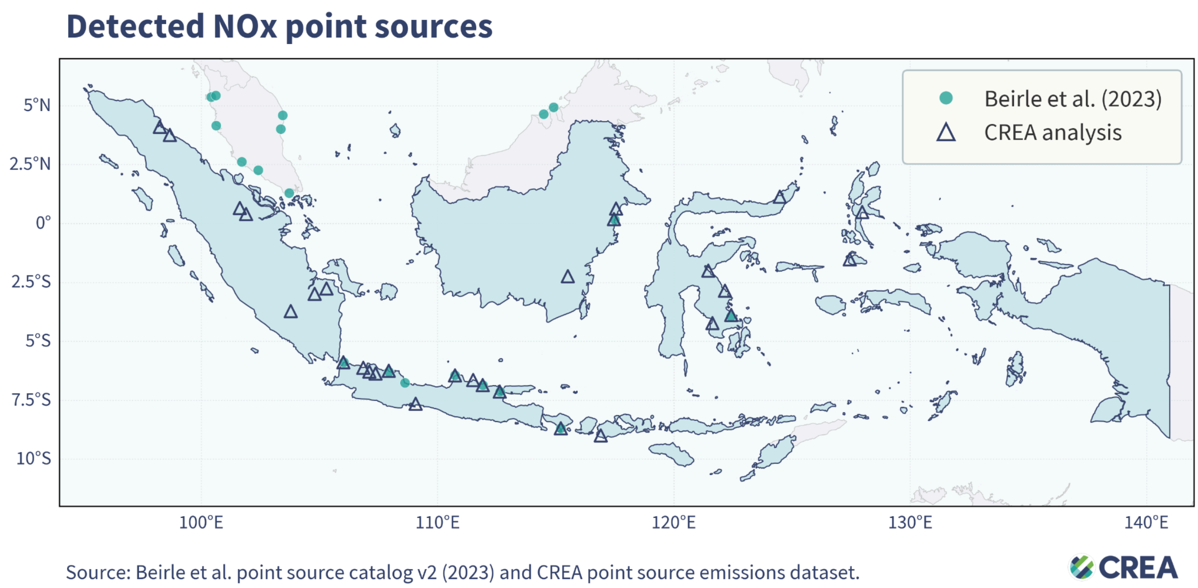

Figure 1. Point sources in the Beirle et al. (2023) catalogue and detected by the CREA analysis.

NO_x emission rates

To evaluate the accuracy of our NO_x emission rates, we compared the calculated emission rates to those estimated by Beirle et al. (2023) and against the reference dataset consisting of NO_x emissions of known point sources based on stack measurements.

To compare our emission rate estimates with those calculated by B23, we ran our emission rate calculation for all point sources in the B23 catalogue that are found within the domains for Indonesia and the US. Following B23, we calculated both the emission rate when averaging from May 2018 to November 2021 as well as for every single year within this time period. Figure 2 shows the comparison between the two datasets. Note that some scatter is expected, as we have used a newer version of the TROPOMI NO_2 data and a different ozone dataset. There have also been updates in the processing, namely we omitted the air mass factor correction, interpolated to a different grid (local UTM instead of global lat-lon), and added the spatial low-pass filter along with the temporal outlier filter.

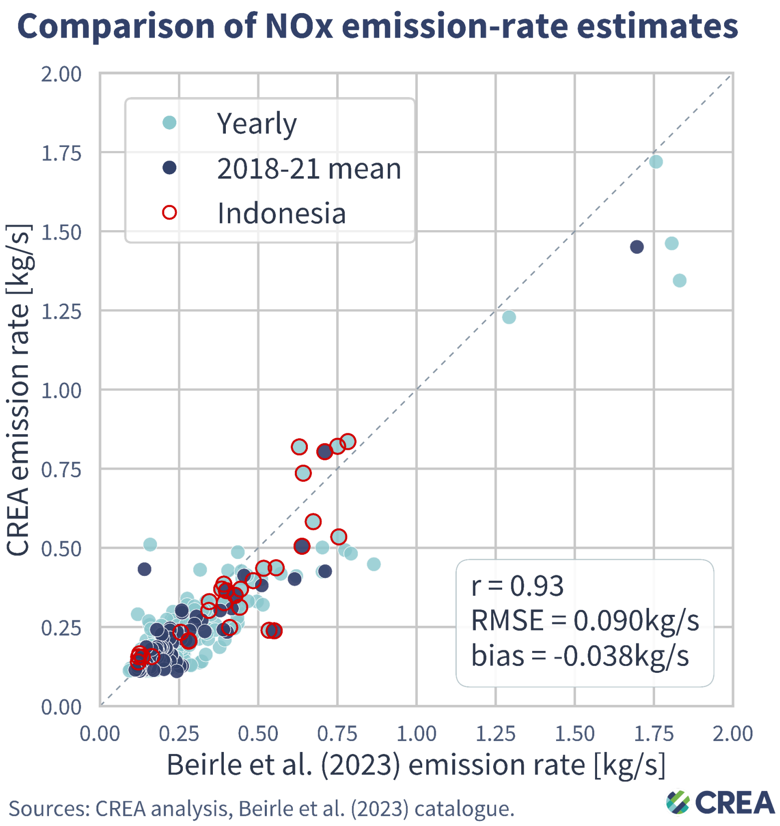

Figure 2. Comparison of emission rates calculated by CREA and Beirle et al. (2023), comparing estimates for the same locations and same time periods. The point sources located in Indonesia are highlighted in red.

To ensure that our updates to the method did not reduce the accuracy of emission estimates, we also compare our estimates with the US EPA dataset used as a reference. To allow comparison with the results of B23, the same time period and locations of point sources as in their catalogue were used. Then, we searched the US EPA dataset for emitters and selected all facilities within a 4 km radius of the satellite-identified point sources. We excluded all locations where the total capacity of the power plants was under 1000 MW, as their emissions would be classified as minor. This resulted in 39 matches. Figure 3 shows the comparison of our satellite-based emission rates with the reference datasets, along with data from B23. The accuracy of the CREA results is comparable to that of the original method.

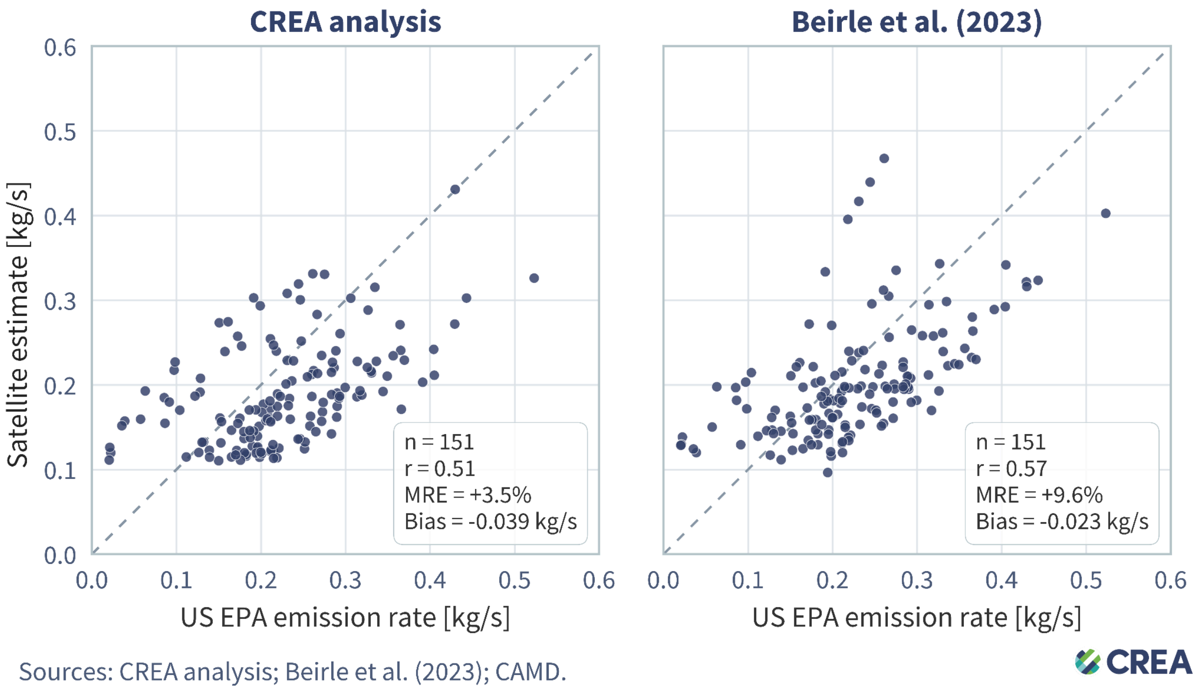

Figure 3. Comparison of emission rates calculated by CREA and Beirle et al. (2023), comparing estimates for the same locations and same time periods.

References

Beirle, S., Borger, C., Dörner, S., Li, A., Hu, Z., Liu, F., Wang, Y., & Wagner, T. (2019). Pinpointing nitrogen oxide emissions from space. *Science Advances*, *5*(11). https://doi.org/10.1126/sciadv.aax9800

Beirle, S., Borger, C., Jost, A., & Wagner, T. (2023). Improved catalog of NO_x point source emissions (version 2). *Earth System Science Data*, *15*(7), 3051–3073. https://doi.org/10.5194/essd-15-3051-2023

Copernicus Atmosphere Monitoring Service. (2020a). *CAMS global reanalysis (EAC4)* [Dataset]. ECMWF. https://doi.org/10.24381/D58BBF47

Copernicus Atmosphere Monitoring Service. (2020b). *CAMS global reanalysis (EAC4) monthly averaged fields* [Dataset]. ECMWF. https://doi.org/10.24381/FD75FFF2

Copernicus Climate Change Service. (2023). *Complete ERA5 global atmospheric reanalysis* [Dataset]. Copernicus Climate Change Service (C3S) Climate Data Store (CDS). https://doi.org/10.24381/CDS.143582CF

de Foy, B., & Schauer, J. J. (2022). An improved understanding of NOx emissions in South Asian megacities using TROPOMI NO2 retrievals. *Environmental Research Letters*, *17*(2), 024006. https://doi.org/10.1088/1748-9326/ac48b4

Dickerson, R. R., Stedman, D. H., & Delany, A. C. (1982). Direct measurements of ozone and nitrogen dioxide photolysis rates in the troposphere. *Journal of Geophysical Research: Oceans*, *87*(C7), 4933–4946. https://doi.org/10.1029/JC087iC07p04933

D.Kovács, D., Musial, J., Bojanowski, J., Clarijs, D., De La Mar, J., & Zlinszky, A. (2026). Copernicus Data Space Ecosystem establishes public cloud processing for earth observation data. *Scientific Data*, *13*(1), 537. https://doi.org/10.1038/s41597-026-06765-8

European Comission. (n.d.). *Legal notice on the use of Copernicus Sentinel Data and Service Information*. Retrieved https://sentinels.copernicus.eu/documents/247904/690755/Sentinel_Data_Legal_Notice

European Space Agency. (2021). *TROPOMI Level 2 Nitrogen Dioxide* [Dataset]. https://doi.org/10.5270/S5P-9bnp8q8

Inness, A., Ades, M., Agustí-Panareda, A., Barré, J., Benedictow, A., Blechschmidt, A.-M., Dominguez, J. J., Engelen, R., Eskes, H., Flemming, J., Huijnen, V., Jones, L., Kipling, Z., Massart, S., Parrington, M., Peuch, V.-H., Razinger, M., Remy, S., Schulz, M., & Suttie, M. (2019). The CAMS reanalysis of atmospheric composition. *Atmospheric Chemistry and Physics*, *19*(6), 3515–3556. https://doi.org/10.5194/acp-19-3515-2019

IUPAC. (2013). *IUPAC Task Group on Atmospheric Chemical Kinetic Data Evaluation – Data Sheet NOx24* [Dataset]. https://iupac-aeris.ipsl.fr/datasheets/pdf/NOx24.pdf

Koene, E. F. M., Brunner, D., & Kuhlmann, G. (2024). On the Theory of the Divergence Method for Quantifying Source Emissions From Satellite Observations. *Journal of Geophysical Research: Atmospheres*, *129*(12), e2023JD039904. https://doi.org/10.1029/2023JD039904

Lange, K., Richter, A., Bösch, T., Zilker, B., Latsch, M., Behrens, L. K., Okafor, C. M., Bösch, H., Burrows, J. P., Merlaud, A., Pinardi, G., Fayt, C., Friedrich, M. M., Dimitropoulou, E., Van Roozendael, M., Ziegler, S., Ripperger-Lukosiunaite, S., Kuhn, L., Lauster, B., … Lee, H. (2024). Validation of GEMS tropospheric NO_2 columns and their diurnal variation with ground-based DOAS measurements. *Atmospheric Measurement Techniques*, *17*(21), 6315–6344. https://doi.org/10.5194/amt-17-6315-2024

Lange, K., Richter, A., & Burrows, J. P. (2022). Variability of nitrogen oxide emission fluxes and lifetimes estimated from Sentinel-5P TROPOMI observations. *Atmospheric Chemistry and Physics*, *22*(4), 2745–2767. https://doi.org/10.5194/acp-22-2745-2022

Lange, K., Richter, A., Schönhardt, A., Meier, A. C., Bösch, T., Seyler, A., Krause, K., Behrens, L. K., Wittrock, F., Merlaud, A., Tack, F., Fayt, C., Friedrich, M. M., Dimitropoulou, E., Van Roozendael, M., Kumar, V., Donner, S., Dörner, S., Lauster, B., … Burrows, J. P. (2023). Validation of Sentinel-5P TROPOMI tropospheric NO_2 products by comparison with NO_2 measurements from airborne imaging DOAS, ground-based stationary DOAS, and mobile car DOAS measurements during the S5P-VAL-DE-Ruhr campaign. *Atmospheric Measurement Techniques*, *16*(5), 1357–1389. https://doi.org/10.5194/amt-16-1357-2023

Sun, K. (2022). Derivation of Emissions From Satellite-Observed Column Amounts and Its Application to TROPOMI NO2 and CO Observations. *Geophysical Research Letters*, *49*(23). https://doi.org/10.1029/2022gl101102

United States Environmental Protection Agency (EPA). (n.d.). *Clean Air Markets Program Data*. Washington, DC: Office of Atmospheric Protection, Clean Air and Power Division. Available from EPA's Air Markets Program Data website: https://campd.epa.gov/.